Analysis and Design of Third-Harmonic Current Injection Active Filter Circuit for the Aircraft

Qingyun Chang, Bo Zhou, Chengjia Lu, and Jiadan Wei, *Senior Member, IEEE*

***Abstract*—Third-harmonic current injection (3rd-HCI) active filter circuit could be utilized to eliminate low-frequency harmonics generated by the three-phase uncontrolled rectifier. However, some problems exist when the circuit operates in the 115 Vrms/400 Hz aircraft power system. The inductor in the 3rd-HCI active filter circuit is not strictly volt-second balance in one switching period, resulting in injection current error and ac line current distortions. The problem is more severe in the 400 Hz power system since the imbalance degree increases with a higher ac frequency. Moreover, the common method to mitigate the ac line current distortions is using a smaller inductor, which will increase the inductor current ripple and high-frequency harmonic components. This article investigates the distortion mechanisms and reveals the relationship between current distortion and volt-second imbalance, and the maximum allowed inductance is determined under every operating point. Then, an improved circuit based on ripple current cancelation technique is proposed to realize quasi-zero ripple in the inductor current and to reduce the high-frequency harmonics in the ac line currents, which extends the operating range of the circuit significantly. Finally, the correctness of analysis and validity of proposed circuit are verified by experimental results based on a 115 Vrms/400 Hz/5 kW prototype.**

***Index Terms*—AC–AC power converter, ac–dc power converter, third-harmonic current injection (3rd-HCI), variable speed constant frequency (VSCF).**

I. Introduction

THREE-PHASE uncontrolled rectifiers with diodes are usually deployed as the front-end circuit of many ac–dc or ac–ac power converters because of their high efficiency, low costs, and simple structure. However, due to the large harmonics and low power factor, the ac line current is not able to meet the standard [1]. To solve the problems, the third-harmonic current injection (3rd-HCI) active filter circuit [1], is proposed to get sinusoidal ac line currents [2], [3], [4]. As illustrated in Fig. 1, an active current injection bridge and an inductor are employed to create third-harmonic current, then the third-harmonic current is fed into the ac line that has the smallest absolute value of three-phase input voltages by using one of the three bidirectional switches. For clarity, the combination of the uncontrolled rectifier and 3rd-HCI active filter circuit is named as 3rd-HCI active filter rectifier in this article [1].

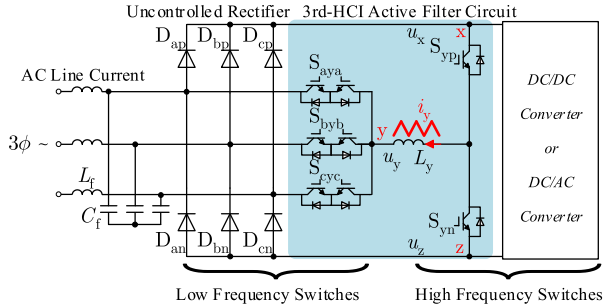

Fig. 1. 3rd-HCI active filter rectifier topology, combining an uncontrolled rectifier and a 3rd-HCI active filter circuit.

The output voltage of 3rd-HCI active filter rectifier is determined directly by the uncontrolled rectifier and is a six-pulse shape. Therefore, the back-end converter should be added to regulate output voltage and to obtain constant power consumption. In [5], a simple buck converter is added to form the three-phase ac–dc converter, and the high efficiency is verified by experiment results. A three-phase ac–ac power converter is constructed by cascading a voltage source inverter with the 3rd-HCI active filter rectifier [6]. Due to the similar characteristics compared to the matrix converter, such as no electrolytic capacitor, it is named as 3rd-HCI two-stage matrix converter. Furthermore, except for the sinusoidal ac line current regulation ability, the input reactive power control ability is also verified in [6]. The input displacement angle can vary within $\pm\pi/2$ in theory.

Compared with the general two-level boost-type rectifier and the three-level Vienna rectifier, the main advantages of the rectifier in Fig. 1 are the low current stress in the 3rd-HCI active filter circuit and the low switching frequency of diodes and bidirectional switches, which contributes to less switching loss and higher efficiency. Besides, the common PiN diodes rather than the Schottky diodes can also be used in the rectifier since the diode reverse recovery is removed. Compared with the Schottky diodes, the PiN diodes have lower costs and could effectively reduce the drift region resistance via conductivity modulation. This makes the rectifier promising in high-voltage applications [7]. In addition, the heat sink volume can be reduced and the dc-link energy storage capacitor is removed from the 3rd-HCI active filter rectifier. Only the small capacitors are employed

Manuscript received 5 October 2023; revised 28 December 2023; accepted 1 February 2024. Date of publication 15 February 2024; date of current version 20 March 2024. This work was supported by the Key Project of National Natural Science Foundation of China under Grant 51737006. Recommended for publication by Associate Editor J. Biela. *(Corresponding author: Bo Zhou.)*

The authors are with the Jiangsu Key Laboratory of New Energy Generation and Power Conversion, College of Automation Engineering, Nanjing University of Aeronautics and Astronautics, Nanjing 210016, China (e-mail: changqy@nuaa.edu.cn; zhoubo@nuaa.edu.cn; nuaahmlcj@nuaa.edu.cn; weijiadan@nuaa.edu.cn).

Color versions of one or more figures in this article are available at https://doi.org/10.1109/TPEL.2024.3366157.

Digital Object Identifier 10.1109/TPEL.2024.3366157

to filter the high-frequency harmonic components, which could reduce the system size and realize high power density.

Considering the features in the above, 3rd-HCI active filter rectifier is suitable for aircraft application, which requires high power density and high efficiency. However, the ac line frequency in the variable speed constant frequency (VSCF) aircraft power system is 400 Hz instead of 50 Hz, which brings new problems to the circuit. For the analysis of the circuit in [5] and [6], it is assumed that the inductor in the 3rd-HCI active filter circuit is volt-second balance in one switching period, which is accurate enough for the case where the ac line frequency is 50 Hz. However, as will be indicated in Section III, the integral of the applied inductor voltage over the whole switching period is nonzero and increases linearly with the higher ac line frequency and load power. The volt-second imbalance would lead to the ac line current distortion and must be considered in the circuit design process, especially for the 400 Hz power system. The common method of suppressing the volt-second imbalance is to reduce the inductance, which causes the disadvantage of higher current ripples. That is, there is a tradeoff between ac line current distortion and higher ripple of inductor current. In some cases, the inductor cannot be designed to meet the requirements of both current ripple and volt-second imbalance degree at the same time, and the only method is to increase the switching frequency or input filter capacitance, which would increase the power loss and reactive currents accordingly.

In order to solve these problems, this article proposes an improved 3rd-HCI active filter circuit based on ripple current cancelation (RCC) technique [8]. According to the principle of RCC, an auxiliary circuit with small volume is added to create ripple current, which has an inverse phase of that in the main circuit, and then the two current ripples are canceled, achieving zero current ripple in the input [9], [10] or output [11], [12]. Although much of the interest of RCC is gathered in dc–dc converters, recently, it is also introduced into the ac power converters for special functions. In [13], the RCC circuit is added to the quasi-Z source inverter to achieve zero output current. A ripple cancelation converter is introduced in the single-phase LED drive to realize flicker-free LED driving with high power factor, high efficiency, and low component cost [14]. In [15], a soft-switched inverter with ultralow output current ripple is obtained due to the current ripple cancelation property. Generally, only the input or the output ripple current is concerned in the design procedure of auxiliary circuit. However, only reducing the ripple of inductor current is not enough for the active current injection bridge, reducing the current ripples in the switches ($S_{\rm yp}$ and $S_{\rm yn}$) is also important otherwise they will increase the high-frequency harmonic components of ac line currents.

The main contributions of this article are twofold.

1) The relationship between the volt-second imbalance and the ac line current distortion is investigated, and the maximum allowed inductance value is given for every operating point.
2) An improved 3rd-HCI active filter circuit based on RCC technique is proposed, whose design only needs to consider the volt-second imbalance constraint, thus extending the operation region significantly.

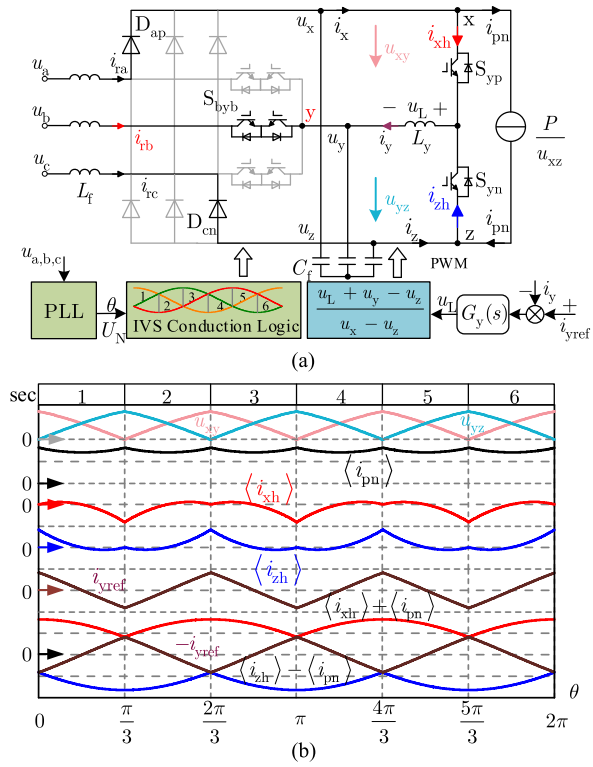

Fig. 2. (a) Equivalent circuit in sector 1 and control strategy. (b) Typical waveforms in the 3rd-HCI active filter rectifier.

In this article, a more thorough analysis including the parameter design criteria for the conventional 3rd-HCI active filter circuit is given in Section II. Section III investigates the problem of inductor volt-second imbalance, and analyzes the relationship between the imbalance and the ac line current distortion. Then, the working principle and parameter design criteria of the improved 3rd-HCI active filter circuit are presented in Section IV. In Section V, a 5 kW prototype operating at 115 Vrms/400 Hz is designed to evaluate the analysis. Finally, Section VI concludes this article.

II. Conventional Analysis and Parameter Design Criteria for the 3rd-HCI Active Filter Circuit

The conventional analysis, including the parameter design criteria without considering inductor volt-second imbalance, is presented in this section, the purpose of which is to show the basic operation principle, and to provide theoretical basis for the further analysis.

A. Conventional Analysis for the Circuit

As shown in Fig. 2, the 3rd-HCI active filter circuit is composed of three bidirectional switches, an active current injection bridge, and an inductor. A sinusoidal three-phase voltage without distortion can be expressed by

$$\begin{cases} u_{\rm a}(\theta) = U_{\rm N}\cos(\theta) \\ u_{\rm b}(\theta) = U_{\rm N}\cos(\theta - 2\pi/3) \\ u_{\rm c}(\theta) = U_{\rm N}\cos(\theta + 2\pi/3) \end{cases} \tag{1}$$

TABLE I
TRUTH TABLE FOR THE SWITCHES OF IVS

Sector	Input Voltages	D_{ap}	D_{an}	D_{bp}	D_{bn}	D_{cp}	D_{cn}	Bid Switch
1	$u_a > u_b > u_c$	1	0	0	0	0	1	S_{byb}
2	$u_b > u_a > u_c$	0	0	1	0	0	1	S_{aya}
3	$u_b > u_c > u_a$	0	1	1	0	0	0	S_{cyc}
4	$u_c > u_b > u_a$	0	1	0	0	1	0	S_{byb}
5	$u_c > u_a > u_b$	0	0	0	1	1	0	S_{aya}
6	$u_a > u_c > u_b$	1	0	0	1	0	0	S_{cyc}

where θ is the phase angle and U_N is the input voltage amplitude. The function of the three bidirectional switches is to ensure that the inductor L_y is always connected to an ac line that has the smallest absolute value of three-phase input voltages. In other words, the six diodes and the three bidirectional switches rearrange the three-phase input voltages from the highest to the lowest, and therefore, $u_x > u_y > u_z$ is obtained. That is

$$\begin{cases} u_x = \max(u_a, u_b, u_c) \\ u_z = \min(u_a, u_b, u_c) \\ u_y = \text{mid}(u_a, u_b, u_c) = -u_x - u_z \end{cases}. \tag{2}$$

The uncontrolled rectifier and the three bidirectional switches are also named as input voltage selector (IVS). In order to further reduce the conduction loss in the rectifier, based on [16], the filter capacitors are moved from the input side to the output side of IVS. According to the relations of instantaneous input voltages, the input voltage sectors 1–6 and the conduction logic of IVS are defined in Table I. It can be found that the switching frequency of bidirectional switches is twice the ac line frequency, and the diodes in the rectifier are operated at ac line frequency, resulting in little switching loss and reverse recovery loss in the IVS.

The sinusoidal ac line currents are achieved by the 3rd-HCI active filter circuit. Taking sector 1 ($u_a > u_b > u_c$) as an example, the equivalent circuit and the reference current direction are shown in Fig. 2(a). Ideally, the constant output power P is realized by the back-end circuit, and then the average dc-link current in one switching cycle $<i_{pn}>$, can be expressed as:

$$\langle i_{pn} \rangle = \frac{P}{u_{xz}}. \tag{3}$$

Furthermore, it can be found the input current of phase b, which is denoted as i_{rb}, is equal to the opposite value of third-harmonic injection current i_y, without considering the capacitor current. Supposing that the input currents are sinusoidal and have the same phase with ac line voltage (unity power factor), the reference injection current i_{yref} should satisfy

$$i_{yref} = -i_{rb} = -\frac{2P}{3U_N}\cos\left(\theta - \frac{2\pi}{3}\right) = -I_N \cos\left(\theta - \frac{2\pi}{3}\right) \tag{4}$$

where I_N is the input current magnitude. With the assumption that the integral of the voltage over the whole switching period is zero, application of the principle of volt-second balance to the inductor L_y in the 3rd-HCI active filter circuit leads to the following equation:

$$d u_{xy} - (1-d) u_{yz} = 0 \tag{5}$$

where d is the duty cycle of S_{yp} in the active current injection bridge. Furthermore, if the actual injection current i_y tracks the reference value i_{yref}, the average currents in S_{yp} and S_{yn}, which are denoted as $<i_{xh}>$ and $<i_{zh}>$, respectively, can be expressed as

$$\langle i_{xh} \rangle = d i_{yref} = \frac{u_{yz}}{u_{xz}} \cdot i_y, \langle i_{zh} \rangle = (1-d) i_{yref} = \frac{u_{xy}}{u_{xz}} \cdot i_y. \tag{6}$$

Based on (3) and (6), the input currents in the other two noninjection phases (phase a and c in sector 1) can be calculated as

$$\begin{aligned} i_{ra} &= \langle i_{xh} \rangle + \langle i_{pn} \rangle = I_N \cos(\theta) \\ i_{rc} &= \langle i_{zh} \rangle - \langle i_{pn} \rangle = I_N \cos\left(\theta + \frac{2\pi}{3}\right). \end{aligned} \tag{7}$$

Therefore, the three-phase input currents are sinusoidal and have the same phase with input voltages, achieving unity power factor. Similar to sector 1, the same results can be obtained for the other sectors. Fig. 2(b) shows the typical waveforms in the 3rd-HCI active filter circuit and the uncontrolled rectifier.

B. Design Criteria for the Conventional Circuit

The inductor L_y and the input filter capacitors C_f need to be designed for the conventional circuit. For the inductor L_y, the ripple of the inductor current has been analyzed in [5] and [6]. The ripple current magnitude Δi_y is a function of the input voltage phase θ. In sector 1 ($0<\theta<\pi/3$), Δi_y and can be expressed as

$$\Delta i_y = \frac{\sqrt{3} U_N}{L_y f_s} \cdot \frac{\sin(\theta)\cos(\theta + \pi/6)}{\cos(\theta - \pi/6)} \tag{8}$$

where f_s is the switching frequency. The peak-to-peak ripple current reaches the maximum value when θ is $\pi/6$. At this time, the reference current i_{yref} is zero and the maximum peak-to-peak current ripple Δi_{ymax} can be calculated as

$$\Delta i_{ymax} = \frac{\sqrt{3} U_N}{4 L_y f_s}. \tag{9}$$

If the desired maximum ripple current is δ_i of the maximum inductor current, the inductance should satisfy

$$L_y > \frac{\sqrt{3} U_N}{2 f_s \delta_i I_N}. \tag{10}$$

The capacitance C_f is designed concerning that the capacitor voltage ripple caused by the high-frequency current at rated power should be limited to δ_u of the input voltage amplitude for the converter's safe operation [17]. Generally, δ_u is set as 10%. For the 3rd-HCI active filter rectifier shown in Fig. 2(a), the high-frequency currents across the three capacitors are not the same. On the one hand, for the capacitor connected to node y, only the current ripple in i_y should be considered. This yields

$$C_f > \frac{\sqrt{3}}{32 \delta_u L_y f_s^2}. \tag{11}$$

On the other hand, to estimate the voltage ripple in capacitors connected to node x or node z, the current ripple in i_{xh} and i_{zh} can be neglected for simplicity if the inductor current ripple factor δ_{i} is not high, calculating the current ripple in i_{pn} is accurate enough. Therefore, the capacitance should satisfy

$$C_{\mathrm{f}} > \frac{I_{\mathrm{N}}\left(2-\sqrt{3}M_{\mathrm{v}}\right)}{4\delta_{\mathrm{u}}U_{\mathrm{N}}f_{\mathrm{s}}k_{\mathrm{f}}} \tag{12}$$

where M_{v} is the voltage conversion ratio and k_{f} is the current pulse count of i_{pn} in one switching period. For example, if a voltage source inverter is employed as the back-end circuit and the continuous space vector modulation is adopted, M_{v} is the ratio of the line-to-line output voltage amplitude to the input line-to-line voltage amplitude, and $k_{\mathrm{f}}=2$ is achieved due to the doubled dc-link current pulse count.

The three capacitors should have the same parameter to achieve three-phase reactive power constant. Therefore, the capacitance is the larger value in (11) and (12). It also can be found from (8) that the ripple in i_{y} is not related to i_{yref}. This reveals that the high-frequency harmonics in the ac line currents under light load are primarily from the injection circuit.

III. Error Injection Current and AC Line Current Distortion for 400 Hz Power System

According to the derivation process in Section II, the sinusoidal ac line currents without distortion are obtained with the assumption that the integral of the inductor voltage over the whole switching period is zero. The assumption holds approximately for the public grid but is hard to be satisfied for the aircraft power system where the ac line frequency is 400 Hz due to the higher slope of i_{yref}. Therefore, this section discusses the ac line current expression without neglecting the volt-second imbalance and then investigates the relationship between the imbalance degree and the ac line current distortion. Finally, the maximum allowed inductance value is given based on the calculation results.

A. AC Line Current Expression Considering Inductor Volt-Second Imbalance

It can be seen from Fig. 2(b) that the reference inductor current i_{yref} decreases linearly with a negative slope when the input voltage sector is in 1, 3, 5 and increases linearly with a positive slope when the input voltage sector is in 2, 4, 6. In order to track the reference current, the desired average voltage u_{L}^{*} across the inductor L_{y} in one switching cycle can be well-approximated as follows:

$$u_{\mathrm{L}}^{*}=L_{\mathrm{y}}\frac{di_{\mathrm{yref}}}{dt}\approx\begin{cases}L_{\mathrm{y}}\frac{-I_{\mathrm{N}}/2-I_{\mathrm{N}}/2}{1/6f_{\mathrm{N}}}=-6L_{\mathrm{y}}f_{\mathrm{N}}I_{\mathrm{N}} & \mathrm{sec}=1,3,5\\ L_{\mathrm{y}}\frac{I_{\mathrm{N}}/2-(-I_{\mathrm{N}}/2)}{1/6f_{\mathrm{N}}}=6L_{\mathrm{y}}f_{\mathrm{N}}I_{\mathrm{N}} & \mathrm{sec}=2,4,6\end{cases} \tag{13}$$

where f_{N} is the grid frequency. This reveals that the actual volt-second of the inductor is nonzero. Furthermore, it can be observed that only the positive voltage u_{xy} and the negative voltage $-u_{\mathrm{yz}}$ can be applied to L_{y} in one switching period. Therefore, in order to create the desired average voltage u_{L}^{*}, the voltage $-u_{\mathrm{yz}}$ should be sufficiently negative to decrease the inductor current for sectors 1, 3, 5. Similarly, the voltage

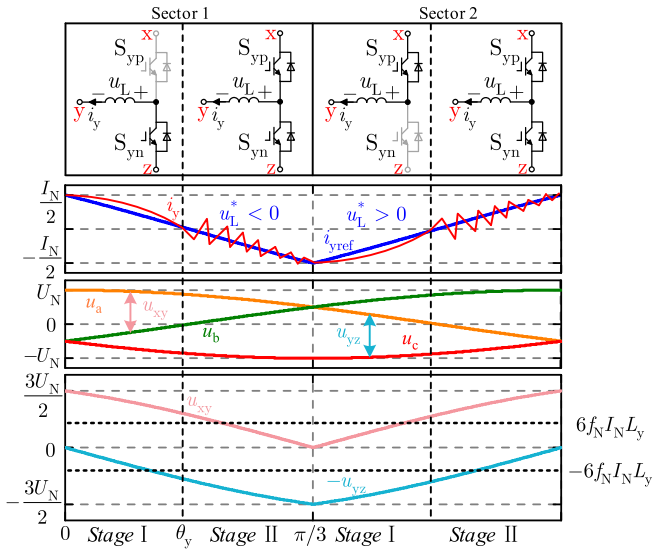

Fig. 3. Two stages of active current injection in one sector.

u_{xy} should be high enough to increase the inductor current i_{y} for sectors 2, 4, 6. Taking sector 1 as an example again, at the beginning of sector 1, considering that u_{yz} is near to zero and $-u_{\mathrm{yz}}<u_{\mathrm{L}}^{*}$, i_{y} cannot track the reference current i_{yref}. Therefore, the whole sector can be divided into two stages by determining whether the actual current follows the reference value, as shown in Fig. 3.

Stage I*:* In this stage, the inductor current cannot follow the given reference since u_{yz} is smaller than the absolute value of u_{L}^{*}, resulting in the controller saturation and the on-state for the low-side switch S_{yn}. In other words, the circuit cannot create the desired negative volt-second in this stage even if the low-side switch is turned-ON continuously. As u_{yz} increases, the inductor current i_{y} drops faster until it tracks the reference at θ_{y}. The equation that describes the inductor current is

$$L_{\mathrm{y}}\frac{di_{\mathrm{y}}}{dt}=-u_{\mathrm{yz}}=-\sqrt{3}U_{\mathrm{N}}\sin(\theta). \tag{14}$$

By solving the equation, the actual injection current and the ac line current of phase b can be obtained

$$i_{\mathrm{rb}}=-i_{\mathrm{y}}=-\frac{I_{\mathrm{N}}}{2}+\frac{\sqrt{3}U_{\mathrm{N}}}{2\pi f_{\mathrm{N}}L_{\mathrm{y}}}\left[1-\cos(\theta)\right]. \tag{15}$$

The error injection current in stage I i_{ye1} is

$$i_{\mathrm{ye1}}=I_{\mathrm{N}}\cos(\theta-2\pi/3)-i_{\mathrm{rb}}. \tag{16}$$

Since the high-side switch S_{yp} is always in the off-state, the current from node x $<i_{\mathrm{xh}}>$ is zero, and the current from node z $<i_{\mathrm{zh}}>$ is equal to i_{y}. This results in the expressions of ac line currents of phases a and c

$$\begin{aligned}i_{\mathrm{ra}}&=I_{\mathrm{N}}\cos(\theta)+I_{\mathrm{N}}\cdot\frac{\sin(\theta)\cos(\theta-2\pi/3)}{\cos(\theta-\pi/6)}\\ i_{\mathrm{rc}}&=I_{\mathrm{N}}\cos(\theta+2\pi/3)+i_{\mathrm{ye1}}-I_{\mathrm{N}}\cdot\frac{\sin(\theta)\cos(\theta-2\pi/3)}{\cos(\theta-\pi/6)}.\end{aligned} \tag{17}$$

It can be seen from (15) and (17) that the three-phase ac line currents are all nonsinusoidal in this stage. Therefore, the time span of this stage θ_y should be reduced as soon as possible, and θ_y can be estimated by solving $i_{ye1}=0$ using 1–cos$\theta \approx \theta^2/2$

$$\theta_y \approx \frac{12L_y f_N I_N}{\sqrt{3}U_N}. \tag{18}$$

The detailed calculation process is given in the Appendix.

Stage II*:* In this stage, the negative voltage $-u_{yz}$ is smaller than u_L^*, the actual current could track the reference, and the two switches in the active current injection bridge alternately conduct in one switching period. The actual duty ratio of S_{yp}, which is denoted as d_{act}, can be calculated by

$$d_{act}(u_x-u_y)+(1-d_{act})(u_z-u_y)=-6L_y f_N I_N. \tag{19}$$

The difference between (19) and (5) lies in the right side of the equation. The actual duty ratio d_{act} must deviate from the ideal duty ratio in (5) due to the volt-second imbalance. In a manner similar to (6), the actual average switch currents $<i_{xh}>$ and $<i_{zh}>$ in one switching cycle can be expressed as

$$\langle i_{xh}\rangle = \frac{u_{yz}+u_L^*}{u_{xz}}\cdot i_y,\ \langle i_{zh}\rangle = \frac{u_{xy}-u_L^*}{u_{xz}}\cdot i_y. \tag{20}$$

Finally, the actual three-phase ac line currents in stage II can be expressed as

$$\begin{aligned} i_{ra} &= I_N\cos(\theta)-\frac{6L_y f_N I_N^2}{\sqrt{3}U_N}\cdot\frac{\cos(\theta-2\pi/3)}{\cos(\theta-\pi/6)}\\ i_{rb} &= -i_{yref}=I_N\cos(\theta-2\pi/3)\\ i_{rc} &= I_N\cos(\theta+2\pi/3)+\frac{6L_y f_N I_N^2}{\sqrt{3}U_N}\cdot\frac{\cos(\theta-2\pi/3)}{\cos(\theta-\pi/6)}. \end{aligned} \tag{21}$$

This reveals that the current in the ac line, which is connected to node y (phase b in sector 1) is sinusoidal as the injection current i_y tracks the reference value i_{yref} without error. However, the other two ac line currents are nonsinusoidal due to the inductor volt-second imbalance. The actual currents in phases a and c contain two terms. The first is the desired sinusoidal ac line current. The second term is the error injection current in stage II i_{ye2} caused by the inductor volt-second imbalance. i_{ye2} is rewritten as

$$i_{ye2}=\frac{6L_y f_N I_N^2}{\sqrt{3}U_N}\cdot\frac{\cos(\theta-2\pi/3)}{\cos(\theta-\pi/6)}. \tag{22}$$

The ratio of the error current to the ac line current amplitude I_N is calculated to evaluate the degree of current distortions

$$\frac{i_{ye2}}{I_N}=\frac{6L_y f_N I_N}{\sqrt{3}U_N}\cdot\frac{\cos(\theta-2\pi/3)}{\cos(\theta-\pi/6)}. \tag{23}$$

In sector 2, the positive voltage u_{xy} should be high enough to increase the inductor current due to the positive reference current slope, as shown in Fig. 3. The analysis result is similar to sector 1, and the corresponding results are omitted.

B. Results Analysis and Maximum Allowed Inductance

Based on the analysis in the above, the error injection current caused by the inductor volt-second imbalance will always exist regardless of whether the actual injection current i_y tracks the reference value, resulting in ac line current distortion. The distortion degree can be evaluated by (18) and (23). It can be observed that there is a common factor δ_y in the two equations

$$\delta_y=\frac{6L_y f_N I_N}{\sqrt{3}U_N}. \tag{24}$$

δ_y is named as volt-second imbalance factor. The influences of δ_y on the ac line currents are summarized as follows.

1) In stage I, the increasing of δ_y causes the time span of stage I to increase. The time span should be reduced as soon as possible.
2) In stage II, higher δ_y leads to larger u_L^*, which causes the actual duty cycle d_{act} to deviate from the ideal duty cycle d and induces the error injection current, as shown in (20) and (23). Although the actual current i_y follows the reference without error, the other two ac line currents are still nonsinusoidal.

Obviously, δ_y and ac line current total harmonic distortion (THD) are closely related. Therefore, δ_y is an important parameter for the 3rd-HCI active filter circuit. For a given application, the f_N, I_N, and U_N are constant, and then only the inductance L_y can be designed to limit current distortion. This yields

$$L_y<\frac{\sqrt{3}U_N\delta_y}{6f_N I_N}. \tag{25}$$

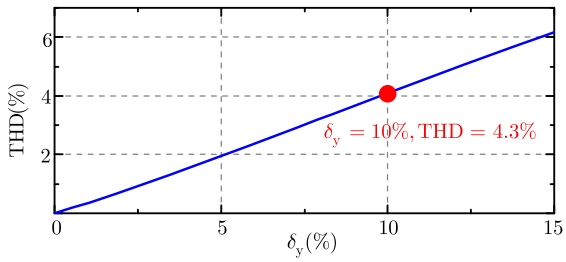

Fig. 4. AC line current THD, as a function of δ_y.

Fig. 4 shows the ac line current THD under different δ_y by FFT analysis, using the calculation results in (15) and (17) and (21). It can be seen that δ_y and THD are strongly linear since all the error currents increase linearly with δ_y. Considering that the THD of ac line currents is limited to 5%, δ_y should not exceed 10%. Generally, δ_y is quite small (<1%) and can be neglected for the 230 V/50 Hz public grid. As a result, the purely sinusoidal ac line currents are still obtained in [5], [6]. However, for the 115 V/400 Hz aircraft power system, the inductor volt-second imbalance factor is 16 times larger than that in the public grid due to the lower voltage and higher ac line frequency, leading to serious current distortion.

Therefore, the inductance should be decreased with ac line frequency increasing, which causes the disadvantage of higher current ripple and higher ac line current high-frequency harmonic components. In other words, for the aircraft applications, the inductance is hard to meet the requirements of (10) and (25) at the same time in the inductor design procedure. At this point, the input filter capacitance or the switching frequency has to be

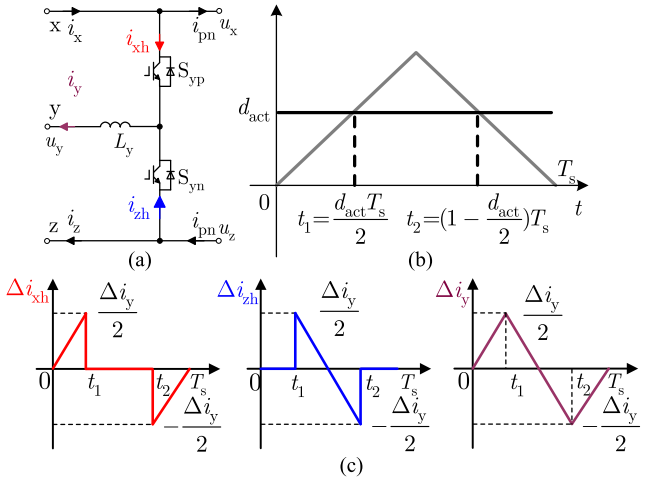

Fig. 5. Topology and waveforms in the conventional circuit. (a) Topology. (b) Carrier waveform. (c) Ripple current waveforms.

increased, which increases the power loss or reduces the power factor.

IV. Improved 3rd-HCI Active Filter Circuit Based on Ripple Cancelation

According to the operation principle of the 3rd-HCI active filter circuit, the three-phase ac line currents are obtained by filtering the switching harmonics in i_x, i_y, and i_z. The expressions of i_x, i_y, and i_z are given by

$$\begin{cases} i_x = i_{xh} + i_{pn} \\ i_z = i_{zh} - i_{pn} \\ i_y = i_{xh} + i_{zh} \end{cases}. \tag{26}$$

i_y, i_{xh}, and i_{zh} are equal to the corresponding average currents $<i_y>$, $<i_{xh}>$, and $<i_{zh}>$, plus the current ripple Δi_y, Δi_{xh}, and Δi_{zh}

$$\begin{cases} i_{xh} = \langle i_{xh} \rangle + \Delta i_{xh} \\ i_{zh} = \langle i_{zh} \rangle + \Delta i_{zh} \\ i_y = \langle i_y \rangle + \Delta i_y \end{cases}. \tag{27}$$

The average values of Δi_y, Δi_{xh}, and Δi_{zh} in one switching period are all zero, and the corresponding waveforms are illustrated in Fig. 5(c). The variable Δi_y has been defined in (8). It can be seen that the current ripples are all increased with the inductance decreasing. According to (26), this increases the high-frequency harmonic components in the three-phase ac line currents. It is desired that the inductance value L_y can be decreased without increasing Δi_y, Δi_{xh}, and Δi_{zh}. Therefore, an improved 3rd-HCI active filter circuit based on RCC technique is proposed to achieve quasi-zero ripple in the actual injection current and to reduce the ripple in the currents from nodes x and z.

A. Topology and Working Principle

The improved 3rd-HCI active filter circuit with RCC is shown in Fig. 6(a), two inductors L_m, which are coupled to the inductor L_y are added in the circuit and are connected to the nodes x

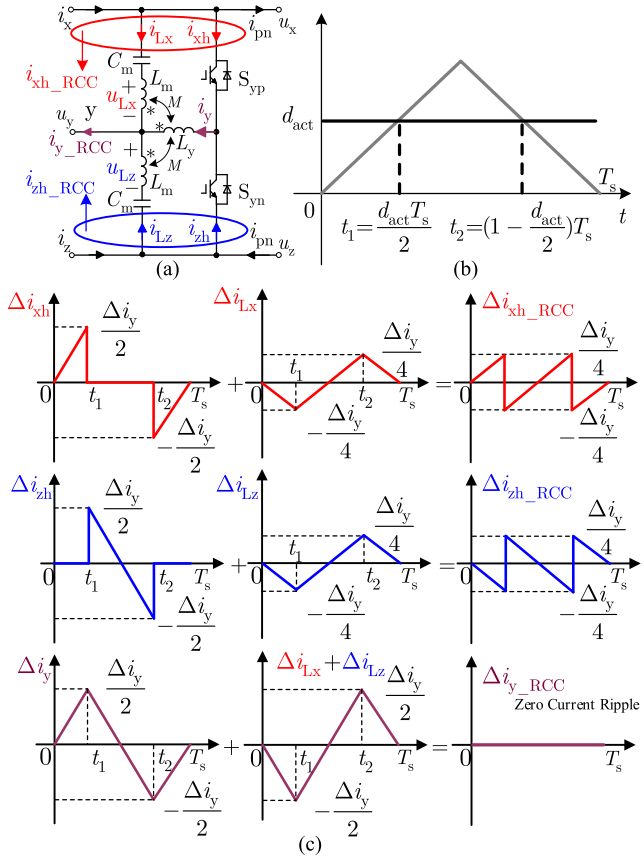

Fig. 6. Topology and waveforms in the improved circuit. (a) Topology. (b) Carrier waveform. (c) Ripple current waveforms.

and z via two blocking capacitors C_m, respectively. The mutual inductance between L_m and L_y is M. Similar to (27), the currents in the two added branches, which are denoted as i_{Lx} and i_{Lz}, can be expressed as

$$\begin{cases} i_{Lx} = \langle i_{Lx} \rangle + \Delta i_{Lx} \\ i_{Lz} = \langle i_{Lz} \rangle + \Delta i_{Lz} \end{cases}. \tag{28}$$

In the steady state, the blocking capacitor voltages in the auxiliary circuit, u_{Lx} and u_{Lz}, are approximately same as the output voltage of IVS, u_{xy} and u_{yz}, respectively. For the conventional dc–dc converter, such as the Buck converter with zero output current ripple [10] and Boost converter with zero input current ripple [12], the voltage applied in the blocking capacitor C_m is constant, therefore, the average currents $<i_{Lx}>$ and $<i_{Lz}>$ are both zero. However, due to the variable voltages u_{xy} and u_{yz} in the 3rd-HCI active filter circuit, the average currents $<i_{Lx}>$ and $<i_{Lz}>$ include the reactive currents that charge and discharge the blocking capacitors, which is different from the dc–dc converter that has constant voltage. The reactive currents should be considered in the parameter design, but they will not influence the ripple characteristic analysis. Therefore, $<i_{Lx}>$ and $<i_{Lz}>$ are neglected here. Furthermore, it should be noted that only the current ripple and the reactive current flow through the auxiliary inductors, therefore, the volume of L_m is very small.

According to Fig. 6(a), the equivalent injection current and the equivalent currents from nodes x and z in the proposed

circuit are

$$\begin{cases} i_{\text{xh\_RCC}} = i_{\text{xh}} + i_{\text{Lx}} \\ i_{\text{zh\_RCC}} = i_{\text{zh}} + i_{\text{Lz}} \\ i_{\text{y\_RCC}} = i_{\text{y}} + i_{\text{Lx}} + i_{\text{Lz}} \end{cases}. \tag{29}$$

The subscript RCC is appended to the variable names, to distinguish the terms from the similarly named terms in the conventional circuit. Furthermore, the corresponding current ripples, which are denoted as $\Delta i_{\text{xh\_RCC}}$, $\Delta i_{\text{zh\_RCC}}$, and $\Delta i_{\text{y\_RCC}}$, are given by

$$\begin{cases} \Delta i_{\text{xh\_RCC}} = \Delta i_{\text{xh}} + \Delta i_{\text{Lx}} \\ \Delta i_{\text{zh\_RCC}} = \Delta i_{\text{zh}} + \Delta i_{\text{Lz}} \\ \Delta i_{\text{y\_RCC}} = \Delta i_{\text{y}} + \Delta i_{\text{Lx}} + \Delta i_{\text{Lz}} \end{cases}. \tag{30}$$

The improved circuit has the same working principle and modulation scheme as the conventional circuit. Therefore, the current waveforms in the switches and inductor L_{y}, as illustrated in the first column of Fig. 6(c), are identical with those in Fig. 5(c). On the other hand, since the blocking capacitor voltages are approximately equal to the output voltage of IVS, u_{xy} and u_{yz}, respectively, the voltages across the two auxiliary inductors are zero. Therefore, the circuit equation can be written as

$$\begin{bmatrix} u_{\text{L}} \\ u_{\text{Lx}} \\ u_{\text{Lz}} \end{bmatrix} = \begin{bmatrix} u_{\text{L}} \\ 0 \\ 0 \end{bmatrix} = \begin{bmatrix} L_{\text{y}} & M & M \\ M & L_{\text{m}} & 0 \\ M & 0 & L_{\text{m}} \end{bmatrix} \begin{bmatrix} di_{\text{y}}/dt \\ di_{\text{Lx}}/dt \\ di_{\text{Lz}}/dt \end{bmatrix}. \tag{31}$$

Solving the equation results in

$$\frac{di_{\text{y}}}{dt} = \frac{L_{\text{m}} u_{\text{L}}}{L_{\text{m}} L_{\text{y}} - 2M^2}, \frac{di_{\text{Lx}}}{dt} = \frac{di_{\text{Lz}}}{dt} = \frac{-M u_{\text{L}}}{L_{\text{m}} L_{\text{y}} - 2M^2}. \tag{32}$$

Substituting (32) into (29) yields an expression for the slope of $i_{\text{y\_RCC}}$ in the improved circuit

$$\frac{di_{\text{y\_RCC}}}{dt} = \frac{di_{\text{y}}}{dt} + \frac{di_{\text{Lx}}}{dt} + \frac{di_{\text{Lz}}}{dt} = \frac{(L_{\text{m}} - 2M) u_{\text{L}}}{L_{\text{m}} L_{\text{y}} - 2M^2}. \tag{33}$$

Finally, the condition for zero current ripple in $i_{\text{y\_RCC}}$ is derived

$$M = \frac{1}{2} L_{\text{m}}. \tag{34}$$

Substituting (34) into (32), the slopes of currents can be rewritten as

$$\frac{di_{\text{y}}}{dt} = \frac{u_{\text{L}}}{L_{\text{eq}}}, \frac{di_{\text{Lx}}}{dt} = \frac{di_{\text{Lz}}}{dt} = \frac{-u_{\text{L}}}{2L_{\text{eq}}}$$

$$L_{\text{eq}} = L_{\text{y}} - M \tag{35}$$

where L_{eq} is the equivalent inductance in the improved 3rd-HCI active filter circuit. When L_{eq} is equal to the inductance in the conventional circuit, the typical current waveforms in the improved circuit are shown in the last column of Fig. 6(c). It should be noted that the condition for zero current ripple is based on the assumption that the blocking capacitor voltages are the same as the output voltages of IVS. In fact, due to the limited capacitance, which is restricted by the reactive power, the voltage ripples would exist in the blocking capacitors. Therefore, the actual injection current $i_{\text{y\_RCC}}$ is quasi-zero ripple rather than ideal zero ripple.

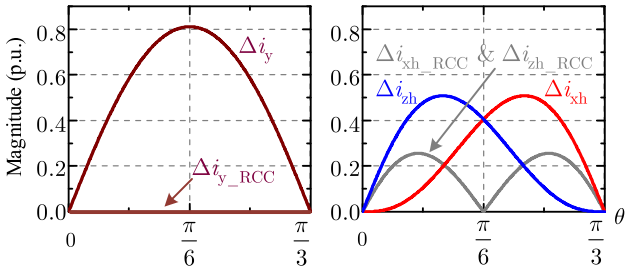

Fig. 7. Magnitude of the first carrier harmonic as a function of θ.

The magnitudes of the first carrier harmonic in the conventional circuit and improved circuit are computed to evaluate the influence on the input filter, using Fourier series applied to the ripple current waveforms during one switching cycle. The magnitude of the first carrier harmonic, which is normalized with respect to Δi_{ymax}, is plotted in Fig. 7 as a function of the input voltage phase θ.

Based on Figs. 5–7, the current ripple characteristics are summarized in the following.

1) Zero current ripple is obtained for $i_{\text{y\_RCC}}$.
2) The maximum magnitude of the first carrier harmonic in $i_{\text{xh\_RCC}}$ and $i_{\text{zh\_RCC}}$ is only half of the magnitude in i_{xh} and i_{zh}. Especially, when θ is nearly $\pi/6$, the first carrier harmonic of $i_{\text{xh\_RCC}}$ and $i_{\text{zh\_RCC}}$ has been reduced to zero as the fundamental frequency of the waveforms has moved toward $2f_{\text{s}}$.

The analysis shows that the improved circuit not only achieves zero ripple in the injection current $i_{\text{y\_RCC}}$ but also reduces the high-frequency harmonics in the currents from nodes x and z ($i_{\text{xh\_RCC}}$ and $i_{\text{zh\_RCC}}$). Therefore, the inductance value of L_{y} can be reduced significantly without increasing the ac line current high-frequency harmonics, and then the current distortion can be removed. It should be noted that the improved circuit only reduces the high-frequency current ripple, and the basic operation principle is the same as that in the conventional circuit, therefore, the control strategy for the conventional circuit is also suitable for the improved circuit, as shown in Fig. 2(a). Furthermore, all the semiconductors in the 3rd-HCI active filter circuit have to block the amplitude of line-to-line voltage $\sqrt{3}U_{\text{N}}$, and the maximum current of semiconductors is only half of the ac line current amplitude.

B. Transfer Function of the Improved Circuit

In order to design the improved circuit, the transfer function should be calculated first. For the input filter, elements L_{f} and C_{f} are chosen to filter the switching harmonics. Besides, a resistor R_{d} is employed in parallel with inductor to damp the resonance. The equivalent circuit, including the damped input filter and the improved 3rd-HCI active filter circuit, is shown in Fig. 8. The transfer function of the circuit is given by

$$G_{\text{y}}(s) = \frac{i_{\text{y\_RCC}}(s)}{i_{\text{y}}(s)} = \frac{1}{2MC_{\text{m}}s^2 + 2C_{\text{m}}Z_{\text{f}}(s)s + 1}$$

$$Z_{\text{f}}(s) = \frac{1}{sC_{\text{f}} + \frac{1}{sL_{\text{f}}} + \frac{1}{R_{\text{d}}}} \tag{36}$$

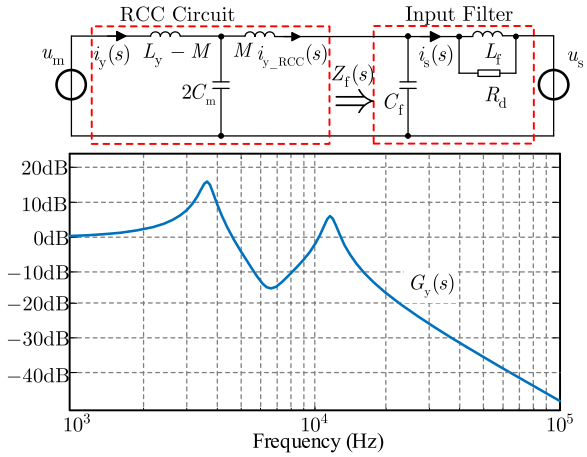

Fig. 8. Equivalent circuit and bode diagram of the improved circuit.

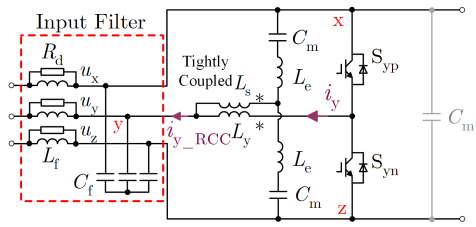

Fig. 9. Implementation of the improved 3rd-HCI active filter circuit based on RCC technique.

where $G_y(s)$ and $Z_f(s)$ are the transfer function of the RCC circuit and the output impedance of input filter, respectively, and then the attenuation characteristic is plotted in Fig. 8. On the one hand, it can be seen that the improved circuit induced an extra resonant frequency due to L_m and C_m. Fortunately, the resonance can be damped owing to the original damping resistor R_d. On the other hand, the RCC circuit is equivalent to an *LCL* filter, therefore, the extra attenuation can be obtained compared to the conventional circuit.

C. Design Criteria

The self-inductance L_m, as shown in Fig. 6(a), can be realized by utilizing the leakage inductance of the winding, achieving the minimum component count. However, the leakage inductance depends on the magnetic circuit, which is hard to be adjusted in the actual experiment. Therefore, the two auxiliary inductors are implemented by using two independent inductors L_e and adding a second winding in L_y. The second winding is tightly-coupled to L_y and has the self-inductance L_s, as shown in Fig. 9. The design criteria of L_y, M, and C_m in Fig. 6(a) are given in this part, and then, L_s and L_e in Fig. 9 can be determined, using the equivalent circuit model of coupled inductor as follows:

$$L_s = \frac{M^2}{L_y}, L_e = L_m - 2L_s = 2M\left(1 - \frac{M}{L_y}\right). \tag{37}$$

1) 3rd-HCI Inductance L_y: Due to the quasi-zero ripple current in the improved circuit, only the volt-second imbalance factor δ_y needs to be considered in the design procedure. Therefore, L_y is determined by (25), and δ_y is limited to 10% based on Fig. 4.

2) Blocking Capacitance C_y: The aim of the capacitors is to block the voltage u_{xy} and u_{yz} and to provide approximately zero voltages for the auxiliary inductors. Therefore, the voltage ripple in C_m, which is caused by the auxiliary inductor ripple current, should be limited to $\delta_c U_N$. Generally, δ_c is set to 5%, achieving a tradeoff between voltage ripple and capacitor volume. Based on (35), the ripple current of each capacitor is half of that in the inductor L_y. Hence, the blocking capacitance is given by

$$C_m > \frac{\sqrt{3}}{64\delta_c L_y f_s^2}. \tag{38}$$

Furthermore, as mentioned in (28), the blocking capacitor voltages u_{xy} and u_{yz} are variable instead of constant, which induces reactive currents $<i_{Lx}>$ and $<i_{Lz}>$

$$\begin{aligned}\langle i_{Lx}\rangle &= C_m\frac{du_{xy}}{dt} \approx \begin{cases} 9C_mU_Nf_N & \text{sec} = 1,3,5 \\ -9C_mU_Nf_N & \text{sec} = 2,4,6 \end{cases} \\ \langle i_{Lz}\rangle &= C_m\frac{d(-u_{yz})}{dt} \approx \begin{cases} 9C_mU_Nf_N & \text{sec} = 1,3,5 \\ -9C_mU_Nf_N & \text{sec} = 2,4,6 \end{cases}. \end{aligned} \tag{39}$$

On the one hand, the induced reactive currents are unbalanced for the three-phase system, therefore, an extra capacitor that has the same capacitance value as the blocking capacitor should be added in the dc-link to balance three-phase reactive power, as shown in Fig. 9. On the other hand, the high-frequency harmonic components of ac line currents are reduced significantly, then the input capacitance in the improved circuit can be reduced to ensure the same total capacitance

$$C_f = \frac{I_N\left(2 - \sqrt{3}M_v\right)}{4\delta_u U_N f_s} - C_m. \tag{40}$$

3) Mutual Inductance M: It can be seen from (39) that the reactive current direction in the auxiliary inductor is changed after input voltage sector switching. Considering that the inductor current cannot be changed instantaneously, then the time constant for L_m and C_m should be small enough to ensure that the reactive current direction can be changed quickly. This yields

$$\frac{1}{2\pi\sqrt{L_mC_m}} = \frac{1}{2\pi\sqrt{2MC_m}} > (3 \sim 5)6f_N. \tag{41}$$

Besides, the actual injection current is not ideal zero ripple current due to the limited blocking capacitance C_m. The actual current ripple factor δ_i' can be obtained by multiplying the current ripple in i_y and the attenuation of RCC circuit

$$\delta'_i = \frac{\sqrt{3}U_N}{4f_sI_N(L_y - M)}|G_y(j\omega)|_{\omega=2\pi f_s}. \tag{42}$$

This should be smaller than the desired current ripple factor, such as 20%. The mutual inductance should satisfy the two constraints at the same time. Finally, L_s and L_e are obtained by (37). The flow chart of the circuit design is shown in Fig. 10.

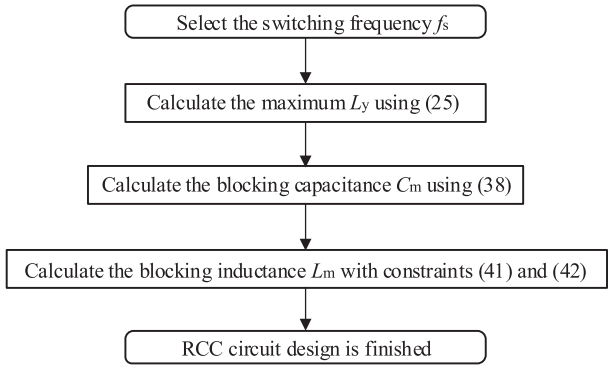

Fig. 10. Flow chart of the circuit design.

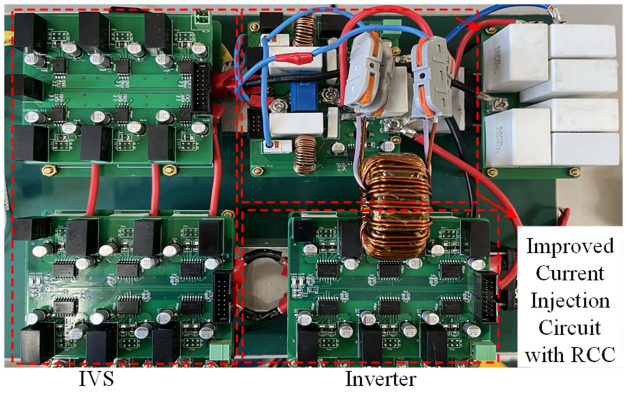

Fig. 11. Experimental platform of the improved 3rd-HCI active filter circuit based on the RCC technique.

V. Experimental Evaluation

A 5 kW prototype operating at 115 Vrms/400 Hz, as shown in Fig. 11, is established to verify the analysis. A voltage source inverter is connected to the dc-link to form a three-phase ac–ac converter. The fundamental frequency of injection current is 1200 Hz. To ensure the low control error, the carrier ratio is selected as 30, resulting in the 36 kHz switching frequency. For the conventional 3rd-HCI active filter circuit without concerning volt-second imbalance, according to (10)–(12), if the desired voltage ripple factor δ_u and current ripple factor δ_i are 10% and 20%, the required values of C_f and L_y should be larger than 3.94 μF and 954 μH, respectively.

Finally, 5.0 μF and 900 μH are selected in the experiment. However, the inductance should not exceed 572 μH if the volt-second imbalance factor δ_y constraint is concerned based on (25). It can be observed that the current ripple and inductor volt-second imbalance constraints cannot be satisfied in the conventional circuit at the same time.

For the improved circuit, the two restrictions are easy to be realized due to the reduced current ripple. Here, the inductance of L_y is selected as 300 μH. The capacitance of blocking capacitor C_m is determined by (38), and then 1 μF is chosen, which yields 4 μF for the input capacitor C_f. Considering the reactive current switching time and system stability, the mutual inductance M is selected as 100 μH based on (41) and (42). Finally, according to (37), the inductance of L_s is 33 μH, and the inductance of L_e is 130 μH. All the parameters of the converters are listed in Table II. The inductors employed in the conventional circuit and improved circuit are shown in Fig. 12. Although the auxiliary inductors are added in the improved circuit, the inductance of L_y is reduced significantly. Therefore, the improved circuit would not increase the volume.

TABLE II
Summary List of Components in the Prototype

Variables	Description	Conventional Circuit	Improved Circuit
f_s	Switching Frequency	36 kHz	36 kHz
L_f	Input Filter Inductor	3×150 μH	3×150 μH
C_f	Input Filter Capacitor	3×5.0 μF	3×4.0 μF
R_d	Damping Resistor	3×22 Ω	3×22 Ω
L_y	Current Injection Inductor	900 μH	300 μH
L_e	Auxiliary Inductor	NULL	2×130 μH
C_m	Auxiliary Capacitor	NULL	3×1.0 μF

Fig. 12. Inductors in the (a) improved circuit and (b) conventional circuit.

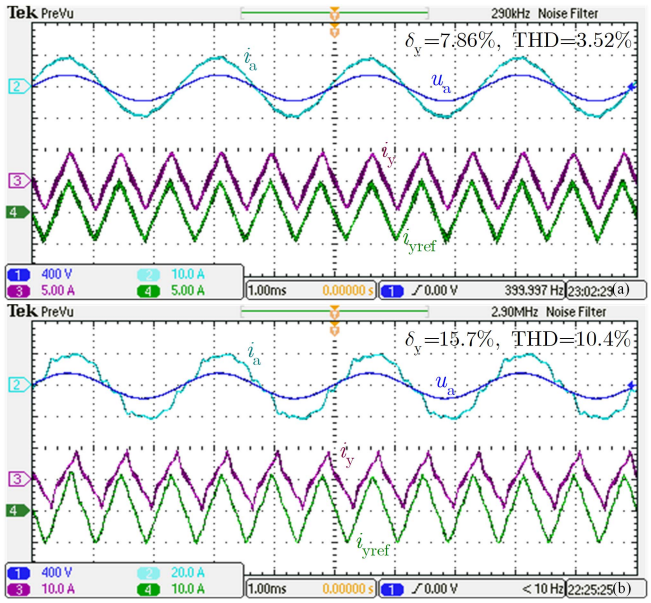

Fig. 13. Experimental results under different inductor volt-second imbalance factors. (a) $P = 2.5$ kW, $\delta_y = 7.86\%$. (b) $P = 5$ kW, $\delta_y = 15.7\%$.

Fig. 13(a) shows the waveforms of the conventional circuit when the load power is 2.5 kW. At this time, the volt-second

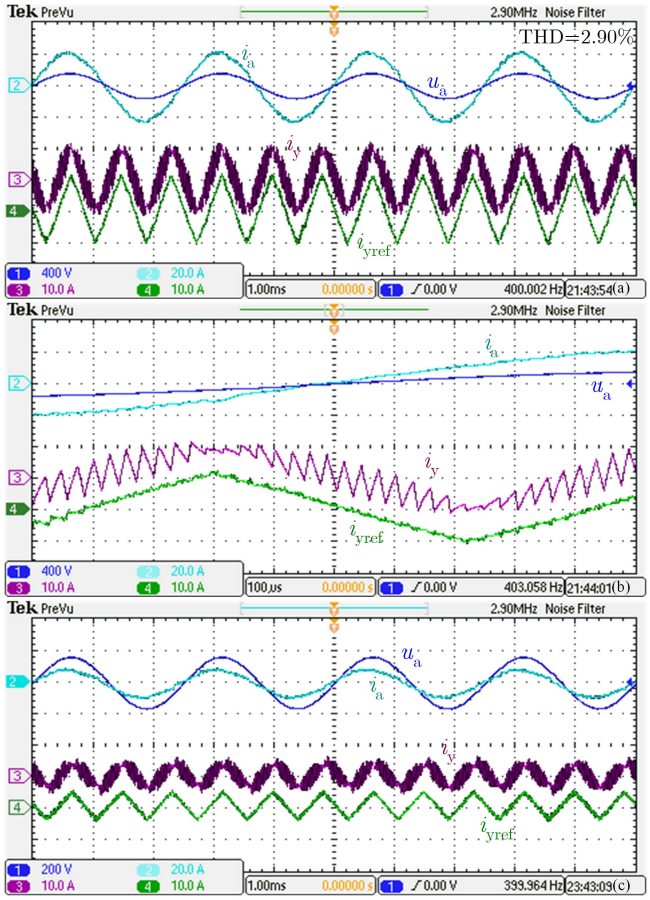

Fig. 14. (a) Experimental result for the conventional circuit in the case where $L_y = 300\ \mu$H and $P = 5$ kW. (b) Zoomed-in window of the waveform. (c) Experimental result at light load (2 kW).

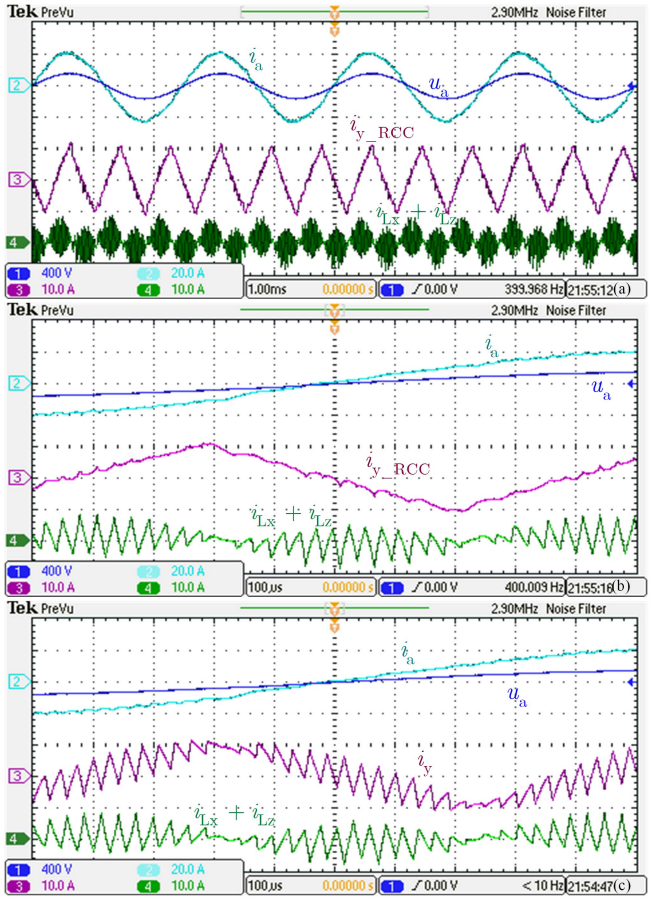

Fig. 15. (a) Experimental result for the improved circuit in the case where $L_y = 300\ \mu$H and $P = 5$ kW. (b) Zoomed-in window of the waveform. (c) Ripple current waveforms at the auxiliary circuit and main circuit.

imbalance factor δ_y is 7.86%, which is within the 10% limitation. Therefore, the ac line current is still sinusoidal with little distortion. Then, the load power is increased from half load to full load (5 kW). In the case where the inductance of L_y is 900 μH, the volt-second imbalance factor δ_y is up to 15.7%, resulting in obvious current distortion, as shown in Fig. 13(b). Based on the analysis in Section III, decreasing the inductance of L_y is a common approach. When the inductance is reduced to 300 μH, the waveforms are shown in Fig. 14(a). The current distortions are removed and the sinusoidal ac line current is obtained again. However, as illustrated in the zoomed-in window of waveforms, cf. Fig. 14(b), the ripple current is increased significantly and the maximum peak-to-peak current ripple is about 10 A, which increases the capacitor voltage ripple and ac line current high-frequency harmonic components. Furthermore, the waveforms at light load (2 kW) in Fig. 14(c) show that the injection current ripple is the same as that under heavy load, and is not related to the magnitude of i_{yref}.

Fig. 15(a) shows the waveform of improved circuit at full load. Compared with Fig. 14(a), the ac line current distortion is also removed. Furthermore, owing to the RCC technique, the current ripple in the improved circuit is reduced to nearly zero. Indeed, the actual current ripple is not ideally zero, and the glitch in the actual current can be observed in Fig. 15(b) due to the limited blocking capacitors. However, the high-frequency harmonic components have been attenuated sufficiently, and the glitch can be filtered by the input LC filter easily. The zoomed-in window in Fig. 15(c) shows that the ripple current waveform (green line) created by the auxiliary circuit has the inverse phase with that in the main power circuit. The experiment results show that the inductance in the improved circuit can be reduced to remove the current distortion caused by the inductor volt-second imbalance without improving the current ripple.

Furthermore, in more electric aircraft, the operating frequency can be as high as 800 Hz. The analysis and design method should be extended to 800 Hz. As mentioned in the above, the injection current in the improved circuit is quasi-zero ripple rather than ideal zero ripple since the blocking capacitance C_m is not infinite due to the limitation of reactive current amplitude and the reactive current direction change after input voltage sector switching. As the ac line frequency increases, the blocking capacitance C_m must be reduced to decrease the reactive current, which also reduced the attenuation of RCC circuit and then increases the current ripple in i_{y_RCC}. Fig. 16 is the experimental results. Due to the higher ac line frequency, the inductance of L_y, and the capacitance of C_m are decreased to 200 μH and 0.47 μF, respectively. Comparison of Fig. 16(a) and (b) reveals that the current ripple in the improved circuit is still decreased

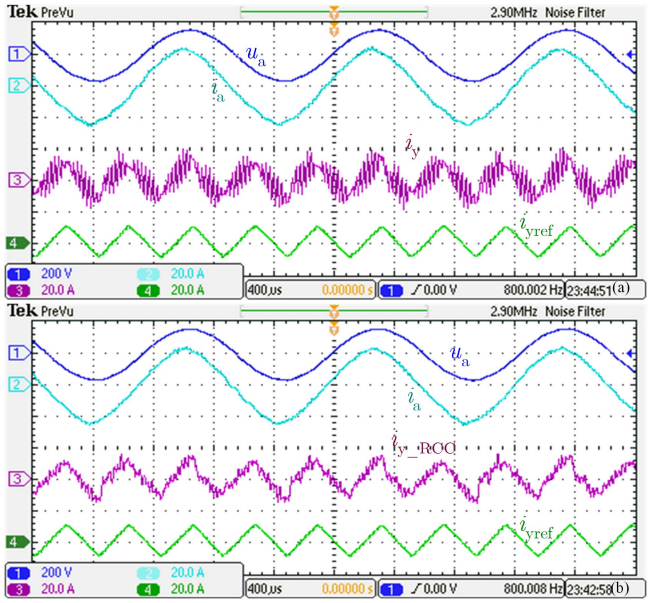

Fig. 16. Experimental result in the case where the ac line frequency is 800 Hz. (a) Conventional circuit. (b) Improved circuit.

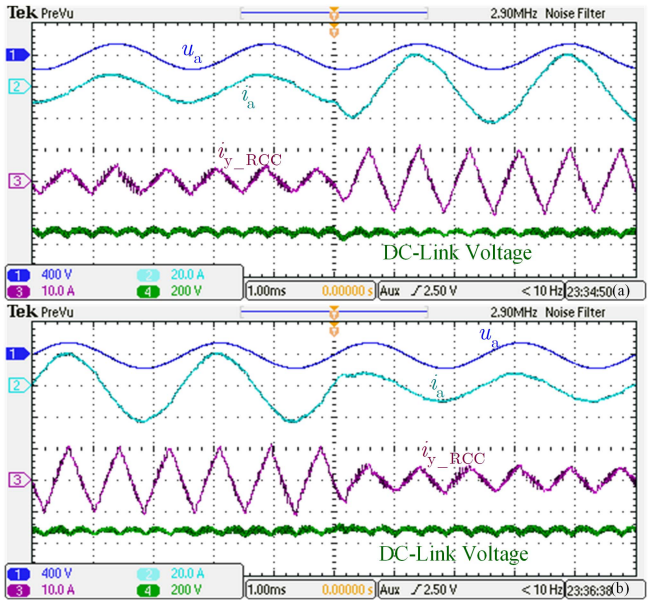

Fig. 17. Experimental results for the improved circuit in (a) load step-up process and (b) load step-down process.

even though the actual injection current is not ideal zero ripple. However, the current ripple in Fig. 16(b) is significantly larger than that in Fig. 15(b). This reveals that there is still a tradeoff in the improved circuit.

The waveforms of dynamic process are shown in Fig. 17. The load power steps up from 2 to 5 kW and then steps down from 5 to 2 kW. The regulation time is about 500 μs, which verifies the operating performance for the improved injection circuit.

Finally, the efficiency curve and ac line current THD curve are plotted in Fig. 18 as a function of load power. In this three-phase ac–ac prototype, the Si-IGBTs and Si-Diodes are employed in the IVS to reduce the costs, and the 40 mΩ SiC-MOSFETs are used

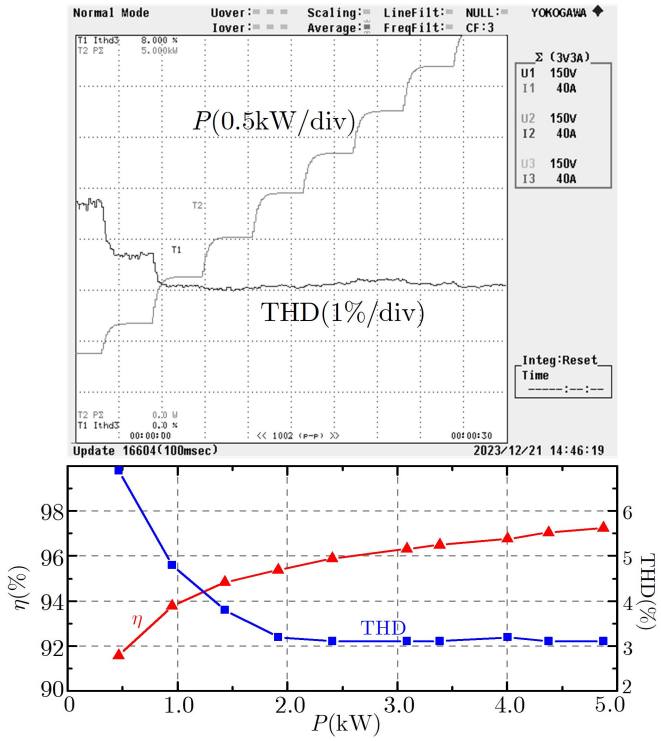

Fig. 18. Prototype efficiency and AC line current THD curves as a function of load power.

to build the active current injection bridge and the voltage source inverter. The peak efficiency is above 97% at rated operating point. Considering the efficiency of voltage source inverter is about 98%, the efficiency in the front-end circuit is about 99%, which demonstrates the high efficiency due to the characteristic of the 3rd-HCI active filter circuit.

VI. Conclusion

In this article, the 3rd-HCI active filter circuit is analyzed and designed for the 115 V/400 Hz aircraft power system. The conclusions are summarized in the following.

1) The volt-second applied to the inductor in the 3rd-HCI active filter circuit is nonzero in one switching period. The volt-second imbalance increases with higher ac line frequency, and then results in the ac line current distortion. Based on the analysis results, the ac line current THD increases linearly with the inductor volt-second imbalance factor. The method of reducing inductance would cause larger inductor current ripples. For some cases, the design of inductor is not able to fulfill the requirements of volt-second imbalance factor and current ripples simultaneously.
2) The improved circuit with RCC technique realizes quasi-zero current ripple in the injection current and reduces the high-frequency harmonic components in the ac line currents. Therefore, only the inductor volt-second imbalance constraint needs to be considered in the inductor design procedure, which extends the operating range of the converter significantly.

APPENDIX

The actual injection current has been obtained in (15)

$$i_{\mathrm{y}} = \frac{I_{\mathrm{N}}}{2} - \frac{\sqrt{3}U_{\mathrm{N}}}{2\pi f_{\mathrm{N}} L_{\mathrm{y}}}\left[1-\cos(\theta)\right]. \tag{A1}$$

Using the equivalent infinitely small 1-cos(θ)≈θ^2/2, i_{y} can be written as

$$i_{\mathrm{y}} \approx \frac{I_{\mathrm{N}}}{2} - \frac{\sqrt{3}U_{\mathrm{N}}}{4\pi f_{\mathrm{N}} L_{\mathrm{y}}}\theta^2. \tag{A2}$$

In stage I, the value θ is not very large, therefore, the approximation is adequate enough. The reference value i_{yref} decreases linearly with a negative slope. It can be seen from Fig. 3 that the slope is about a constant, therefore, the reference can be expressed as

$$i_{\mathrm{yref}} = -I_{\mathrm{N}}\cos\left(\theta - \frac{2\pi}{3}\right) \approx \frac{I_{\mathrm{N}}}{2} - \frac{3I_{\mathrm{N}}}{\pi}\theta. \tag{A3}$$

At θ_{y}, i_{y} is equal to i_{yref}, that is, (A2) is equal to (A3). This yields

$$\theta_{\mathrm{y}} = \frac{12L_{\mathrm{y}}f_{\mathrm{N}}I_{\mathrm{N}}}{\sqrt{3}U_{\mathrm{N}}}. \tag{A4}$$

REFERENCES

[1] J. W. Kolar and T. Friedli, "The essence of three-phase PFC rectifier systems—Part I," *IEEE Trans. Power Electron.*, vol. 28, no. 1, pp. 176–198, Jan. 2013.

[2] H. Yoo and S.-K. Sul, "A novel approach to reduce line harmonic current for a three-phase diode rectifier-fed electrolytic capacitor-less inverter," in *Proc. 24th Annu. IEEE Appl. Power Electron. Conf. Expo.*, 2009, pp. 1897–1903.

[3] H. Yoo and S.-K. Sul, "A new circuit design and control to reduce input harmonic current for a three-phase AC machine drive system having a very small DC-link capacitor," in *Proc. 25th Annu. IEEE Appl. Power Electron. Conf. Expo.*, 2010, pp. 611–618.

[4] N. Vazquez, H. Rodriguez, C. Hernandez, E. Rodriguez, and J. Arau, "Three-phase rectifier with active current injection and high efficiency," *IEEE Trans. Ind. Electron.*, vol. 56, no. 1, pp. 110–119, Jan. 2009.

[5] T. B. Soeiro, F. Vancu, and J. W. Kolar, "Hybrid active third-harmonic current injection mains interface concept for DC distribution systems," *IEEE Trans. Power Electron.*, vol. 28, no. 1, pp. 7–13, Jan. 2013.

[6] H. Wang et al., "Two-stage matrix converter based on third-harmonic injection technique," *IEEE Trans. Power Electron.*, vol. 31, no. 1, pp. 533–547, Jan. 2016.

[7] X. She, A. Q. Huang, Ó. Lucía, and B. Ozpineci, "Review of silicon carbide power devices and their applications," *IEEE Trans. Ind. Electron.*, vol. 64, no. 10, pp. 8193–8205, Oct. 2017.

[8] R. S. Balog and P. T. Krein, "Coupled-inductor filter: A basic filter building block," *IEEE Trans. Power Electron.*, vol. 28, no. 1, pp. 537–546, Jan. 2013.

[9] Y. Gu and D. Zhang, "Interleaved boost converter with ripple cancellation network," *IEEE Trans. Power Electron.*, vol. 28, no. 8, pp. 3860–3869, Aug. 2013.

[10] Y. Zhou and W. Huang, "Single-stage boost inverter with coupled inductor," *IEEE Trans. Power Electron.*, vol. 27, no. 4, pp. 1885–1893, Apr. 2012.

[11] H. Zhu, D. Zhang, Y. Zhou, C. Zhang, and Y. Zhang, "Integrated magnetic Buck–Boost converter with zero output current ripple," *IEEE Trans. Ind. Electron.*, vol. 68, no. 7, pp. 5821–5832, Jul. 2021.

[12] D. Díaz, O. García, J. Á. Oliver, P. Alou, Z. Pavlovic, and J. A. Cobos, "The ripple cancellation technique applied to a synchronous buck converter to achieve a very high bandwidth and very high efficiency envelope amplifier," *IEEE Trans. Power Electron.*, vol. 29, no. 6, pp. 2892–2902, Jun. 2014.

[13] A. Battiston, E.-H. Miliani, S. Pierfederici, and F. Meibody-Tabar, "A novel quasi-Z-source inverter topology with special coupled inductors for input current ripples cancellation," *IEEE Trans. Power Electron.*, vol. 31, no. 3, pp. 2409–2416, Mar. 2016.

[14] P. Fang, Y. Qiu, H. Wang, and Y.-F. Liu, "A single-stage primary-side-controlled off-line flyback LED driver with ripple cancellation," *IEEE Trans. Power Electron.*, vol. 32, no. 6, pp. 4700–4715, Jun. 2017.

[15] S. Bagawade, M. Pahlevani, and P. Jain, "Novel soft-switched three-phase inverter with output current ripple cancellation," *IEEE Trans. Power Electron.*, vol. 38, no. 1, pp. 1232–1248, Jan. 2023.

[16] L. Schrittwieser, J. W. Kolar, and T. B. Soeiro, "Novel SWISS rectifier modulation scheme preventing input current distortions at sector boundaries," *IEEE Trans. Power Electron.*, vol. 32, no. 7, pp. 5771–5785, Jul. 2017.

[17] T. Nussbaumer, M. L. Heldwein, and J. W. Kolar, "Differential mode input filter design for a three-phase buck-type PWM rectifier based on modeling of the EMC test receiver," *IEEE Trans. Ind. Electron.*, vol. 53, no. 5, pp. 1649–1661, Oct. 2006.

Qingyun Chang was born in Yantai, China, in 1993. He received the B.S. degree in electrical engineering from Shandong University, Jinan, China, in 2017. He is currently working toward the Ph.D. degree in electrical engineering with the Nanjing University of Aeronautics and Astronautics, Nanjing, China.

His research interests include the control technology and design of ac–ac converter and starter/generator systems in aerospace.

Bo Zhou was born in Wenzhou, China, in 1961. He received the B.S. degree from Zhejiang University, Hangzhou, China, in 1983, the M.S. degree from Chongqing University, Chongqing, China, in 1986, and the Ph.D. degree from the Nanjing University of Aeronautics and Astronautics (NUAA), Nanjing, China, in 2000, all in electrical engineering.

He is with the NUAA, where he is currently a Professor in Electrical Engineering with the College of Automation Engineering, and is the Director of the Jiangsu Key Laboratory of New Energy Generation and Power Conversion. His research interests include power converter, electrical machine driving systems, and renewable power systems.

Dr. Zhou was the recipient of the State Technological Invention Second-Class Award in 2009, the Geneva International Invention Gold Award in 2011, and the Defense Technological Invention First Prize in 2008.

Chengjia Lu was born in Nantong, Jiangsu, China, in 1995. He received the B.S. degree in electrical engineering in 2017 from the Nanjing University of Aeronautics and Astronautics, Nanjing, China, where he is currently working toward the Ph.D. degree in electrical engineering.

His main research interests include matrix converters and its applications in wind energy systems and aerospace power systems.

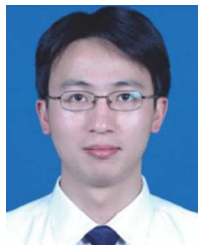

Jiadan Wei (Senior Member, IEEE) was born in Danyang, China, in 1981. He received the B.S. and Ph.D. degrees in electrical engineering from the Nanjing University of Aeronautics and Astronautics (NUAA), Nanjing, China, in 2003 and 2009, respectively.

Since 2009, he has been a Member of the Faculty with the Department of Electrical Engineering, NUAA, where he is currently a Professor with the College of Automation Engineering, NUAA. From 2016 to 2017, he was a Visiting Scholar with the Power Electronics, Machine and Control (PEMC) Research Group, University of Nottingham, Nottingham, U.K. His research interests include aircraft power systems, sensorless control of electric machines, and integrated motor and battery charger for electric vehicles.